2017

Design of Multifunctional Lattice-Frame Materials for Compact Heat Exchangers

K. N. Son
Purdue University

J. A. Weibel
Purdue University, jaweibel@purdue.edu

V. Kumaresan
Purdue University

S. V. Garimella
Purdue University, sureshg@purdue.edu

Design of multifunctional lattice-frame materials for compact heat exchangers[1]

Karen N. Son, Justin A. Weibel, Vellaisamy Kumaresan, Suresh V. Garimella[2]

Cooling Technologies Research Center, an NSF IUCRC
School of Mechanical Engineering
Purdue University, 585 Purdue Mall, West Lafayette, IN 47907 USA

Abstract

Structured porous materials show great potential as extended surfaces in heat-exchange applications that also require design for load-bearing capability. In particular, lattice-frame materials (LFM) are known for their superior strength-to-weight ratio; this work presents a comprehensive experimental and numerical study of fluid flow and heat transfer in porous LFMs. Flow through a periodic unit cell of the material is simulated to characterize the forced-convection performance under hydraulically and thermally fully developed conditions. The performance of LFMs with a tetrahedral ligament configuration is characterized as a function of Reynolds number in the laminar regime ($150 < \text{Re} < 1000$) in terms of Nusselt number and friction factor; the effect of porosity is studied by changing the ligament diameter. Experiments are performed for a subset of porosities to validate the numerical approach. A method is demonstrated for utilizing the simulation results, which assume perfect surface efficiency, to predict the performance of LFMs with non-ideal surface efficiency, based on the conduction resistance of the ligaments. It is shown that the thermal behavior of the ligaments closely matches that of cylindrical fins in cross flow and that this analogy can be used to calculate the overall surface efficiency. The implications of the current results on the design of compact heat exchangers using LFMs is assessed using several conventional performance metrics. Our analysis illustrates the challenges in defining any one universal performance metric for compact heat exchanger design; an appropriate performance metric must be selected that accounts for the particular multifunctional performance characteristics of interest. LFMs are shown to provide the benefits of high-porosity and high surface area-to-volume ratio of materials such as metal foams, while also incurring lower pressure drops and displaying higher structural integrity. This makes them ideal for heat exchangers in aerospace and other applications demanding such multifunctional capabilities. The characterization provided in this study readily allows LFM designs for heat exchanger applications with combined heat-transfer and pressure-drop constraints.

Keywords: Compact heat exchangers; Lattice-frame materials; Multifunctional materials; Forced convection; Porous materials

Nomenclature

A area, m^2

A_{fr} channel frontal area ($H \times W$), m^2

A_t total heat transfer surface area, m^2

c_p gas specific heat, J/(kg K)

d ligament diameter, mm

D_h hydraulic diameter, Equation (2), mm

E friction power expended per surface heat transfer area, Equation (16), W/m^2

f friction factor, Equation (5)

H height, mm

h heat transfer coefficient, W/m^2

j Colburn j factor, Equation (4)

k thermal conductivity, W/(m K)

l ligament length, mm

L length, mm

Nu   Nusselt number, $\mathrm{Nu} = \dfrac{hD_h}{k_g}$

p pressure, Pa

Pr   Prandtl number ($c_p\mu/k$)

Re   Reynolds number, $\mathrm{Re} = \dfrac{\rho u_\infty D_h}{\mu}$

S_x tetrahedron longitudinal pitch, mm

S_y tetrahedron transverse pitch, mm

St   Stanton number, $\mathrm{St} = \dfrac{h}{\rho u_\infty c_p}$

T temperature, K

u velocity, m/s

u_∞ superficial fluid velocity, m/s

V_{uc} total volume of a unit cell, including solid ligament and fluid space, m^3

W width, mm

x axial flow coordinate, mm

y transverse flow coordinate, mm

Greek symbols

ε porosity

ϕ ligament angle of inclination

ρ gas density

μ gas dynamic viscosity

η_f fin efficiency

η_o overall surface efficiency

Subscript

avg average

i,j index

g gas

f fin

s solid

1. Introduction

With the continual increase in power consumption and performance demands under increasingly stringent size constraints in a variety of thermal systems, such as those deployed in electronics thermal management, waste heat recovery, and aerospace applications, there is great need for compact heat exchangers with improved heat dissipation capabilities. Over the last two decades, high-porosity metal foams have been evaluated as a potential heat-exchange medium with high surface area density, low weight, and tortuous coolant flow paths that promote flow mixing and prevent the growth of resistive thermal boundary layers. These metal foams have been investigated extensively in the literature, and simplified models [1-7] and experimental correlations [7-16] for the friction factor and Nusselt number have been developed to predict the pressure drop and heat transfer performance in forced-convection, foam-filled heat exchangers as a function of their geometric parameters. A recent review article by Zhao [17] presents an overview of thermal-hydraulic transport in high-porosity cellular ceramic and metallic foam materials. Though metal foams provide high surface-area-to-volume ratios, they suffer from low bulk thermal conductivity (*e.g.*, 2 to 7 W/(m K) for 90%-porosity aluminum foams in air [17-22]) and high pressure drops that limit their practical applicability in compact heat exchangers [23]. Moreover, metal foams often require additional support structures due to their low mechanical strength and stiffness [24,25].

In recent years, structured porous media known as lattice-frame materials (LFM) have received significant attention owing to their tunable, multifunctional properties. A lattice-frame material consists of a periodic network of cylindrical ligaments of constant cross section, unlike stochastic metal foams which typically have ligaments that vary in diameter along their length. This periodicity and homogeneity gives LFMs an advantage over stochastic metal foams by allowing optimization of the ligament configuration and diameter for specific applications and requirements [27]. With advances in additive manufacturing technologies, LFMs can be fabricated with small-scale feature sizes and three-dimensional ligament arrangements in a variety of possible configurations including square, diamond, tetrahedral, kagome, and pyramidal lattice structures [28-30]. In addition to these different configurations, researchers have also explored various materials (*e.g.*, metal, carbon fiber, and composites) to address a range of multifunctional needs. Xiong *et al.* recently reviewed these LFM structures and their potential applications [31]. Multifunctional load-bearing and effective heat dissipation capabilities have the potential to reduce the volume and weight of heat exchangers because LFMs do not require the separate support and stiffening structures needed by metal foams [32]. This is especially advantageous in aerospace applications where heat exchangers are often used as structural elements [26]. We review below previous studies that investigate pressure drop and convective heat transfer in tetrahedral LFMs.

Lattice-frame materials were first investigated as structural components that provide high compressive strength and resistance to plastic buckling [32,33-36]; subsequently, they have been considered as potential convective heat transfer media. Lu *et al.* compared LFMs against prismatic cores, woven metal textiles, metal foams, and traditional louvered fins [29]. For a load-bearing heat exchanger, LFMs and prismatic core structures outperformed all other options based on a comparison of the heat transferred per unit temperature difference and pressure drop. Using this same metric, Krishnan *et al.* [37] found the overall performance of LFMs to be approximately three times larger than that of stochastic metal foams at similar porosities. In a series of experimental studies by Kim and co-workers [38-40], the pressure drop and heat transfer characteristics of compact heat exchangers composed of tetrahedral LFMs were measured. Local wall temperature measurements revealed the formation of vortices within the structure and that the corresponding local heat transfer coefficients were sensitive to subtle variations in the ligament vertex locations and inclination angles. Owing to their superior mechanical and convective transport characteristics, lattice-frame materials are a viable alternative to stochastic metal foams for heat-exchange applications. Past work has investigated transport in LFMs using either numerical or experimental approaches that analyze the influence of microstructural variations over a limited range. However, the successful adoption of LFMs for heat exchanger design requires an understanding of the particular application needs to which their pressure drop and heat dissipation characteristics can be tailored; singular performance metrics typically considered in past work cannot be used for such tailored design.

In this work, we characterize the performance of lattice-frame materials as a function of porosity using several conventional performance metrics to delineate the specific applications for which they are a suitable heat-exchange medium. We use an integrated simulation and experimental validation approach to systematically investigate the effect of porosity on pressure drop and forced convection heat transfer in LFMs. We also validate a simplified correction factor to account for the finite surface efficiency, which can be used to predict the thermal performance for materials of different thermal conductivity based on the simulation data. Finally, we analyze the results with a focus on the implications of each performance metric on heat exchanger design using LFMs.

2. Lattice-frame material geometry

Lattice-frame materials consist of a periodic network of cylindrical ligaments. We investigate a specific tetrahedral lattice configuration with its ligaments organized in the shape of a tetrahedron, as shown in Figure 1a. In the tetrahedral LFM considered, an equilateral triangular base forms the bottom of each structural unit with cylindrical ligaments arising from each vertex. These three ligaments define the vertical edges of the tetrahedral structure, while the bottom and top ends of the ligaments intersect with

solid walls that sandwich the structure. These two walls form a flow channel in which the ligaments act as an extended surface to enhance heat transfer and add structural support. This LFM structure is fully defined by the height, H, and ligament diameter, d, from which all other characteristic dimensions can be derived (Table 1). The tetrahedral LFM contains repeating units of this tetrahedron structure arranged so that the vertices of each adjacent triangular base connect. A representative unit cell of the tetrahedral LFM consists of a section containing four tetrahedron structures that is twice the tetrahedron longitudinal pitch, S_y, in width and twice the tetrahedron transverse pitch, S_x, in length (Figure 1b).

The tetrahedral lattice-frame material considered is anisotropic, and the flow path differs through the orthogonal x and y orientations as shown in Figure 1c and Figure 1d, respectively. The y orientation has a higher projected flow blockage area relative to the x orientation (both orientations have the same total surface area). The relative differences between these two orientations were quantitatively assessed in Ref. [36] and will not be further addressed; the lower-flow-blockage x orientation is investigated in this study.

3. Modeling approach

3.1. Length scale definitions and non-dimensionalization

The LFM porosity is defined as the ratio of the open volume in the interstices to the total unit-cell volume. The porosity is an important tunable parameter that presents a tradeoff between flow blockage and surface area available for heat transfer. To analyze the influence of porosity, the LFM ligament diameter is varied while holding the overall unit-cell dimensions fixed. The porosity as a function of the ratio of the ligament diameter to the channel height is derived as

$$\varepsilon = 1 - \frac{\sqrt{2}}{2}\pi\left(\frac{d}{H}\right)^2 + \frac{\sqrt{66}+2\sqrt{3}}{9}\left(\frac{d}{H}\right)^3. \tag{1}$$

The definition of hydraulic diameter D_h is selected such that it is consistent with the definition of hydraulic diameter for an empty channel at the limit of 100% porosity,

$$D_h = \frac{4\varepsilon V}{A_s}, \tag{2}$$

which is derived for a tetrahedral LFM as,

$$D_h = \frac{18H^3 - 9\sqrt{2}H\pi d^2 + 2\sqrt{3}\left(2+\sqrt{22}\right)d^3}{9H^2 + 9\sqrt{2}H\pi d - \left(3\sqrt{3}\left(2+\sqrt{22}\right) + \frac{9\sqrt{2}}{2}\arctan\left[\frac{3}{\sqrt{2}}\right]\right)d^2}. \tag{3}$$

5

Using this definition of hydraulic diameter as the characteristic length for the Reynolds number and Nusselt number is a common approach for unified comparison of the fluid-thermal performance between different heat exchanger surface geometries [40].

The Prandtl number, Pr, in combination with the Stanton number, St, forms the non-dimensional Colburn j-factor,

$$j = \text{St} \cdot \text{Pr}^{2/3}. \tag{4}$$

The friction factor is used to quantify the flow resistance in non-dimensional form. The pressure gradient, which accounts for both viscous shear and pressure drag losses, is used as an equivalent total shear force along the flow direction per unit surface area to define the friction factor as

$$f = \frac{\left(-\frac{dp}{dx}\right)D_h}{\frac{1}{2}\rho u^2}. \tag{5}$$

Note that this definition is the conventional Fanning friction factor.

3.2. Computational domain and governing equations

Fully developed laminar flow through a tetrahedral LFM unit cell is simulated. The computational domain (Figure 2) only includes the fluid region in the interstices of the ligaments that compose the lattice-frame material. The respective governing continuity, momentum, and energy equations for steady, periodic, laminar flow through this domain are:

$$\frac{\partial}{\partial x_i}\left(\rho u_i\right) = 0 \tag{6}$$

$$\frac{\partial}{\partial x_j}\left(\rho u_i u_j\right) = -\frac{\partial \hat{p}}{\partial x_i} + \frac{\partial}{\partial x_j}\left(\mu \frac{\partial u_i}{\partial x_j}\right)_i - \frac{\partial \overline{p}}{\partial x_i}e_{L,i} \tag{7}$$

$$\frac{\partial}{\partial x_i}\left(\rho u_i c_p T\right) = \frac{\partial}{\partial x_i}\left(k \frac{\partial T}{\partial x_i}\right) \tag{8}$$

The above equations are written assuming the flow is thermally and hydrodynamically fully developed. For flow through periodic unit-cells, the pressure gradient can be divided into two components, the periodic component $\partial \hat{p}/\partial x_i$ and a linearly varying component $\left(\partial \hat{p}/\partial x_i\right)e_{L,i}$ [41], where $e_{L,i}$ is the ith component of the unit vector in the flow direction. The $\partial \overline{p}/\partial x_i$ term represents the pressure gradient that is assigned across the periodic unit-cell *a priori*, which controls the mass flow rate

6

through the flow domain, and hence, the Reynolds number. In this work, the Reynolds number is varied by controlling this pressure drop term.

3.3. Boundary conditions

Figure 2a shows the boundary conditions employed for the unit-cell model. To predict the global performance of a heat exchange layer comprised of many adjacent periodic unit cells using a single unit-cell simulation domain, periodic boundary conditions are applied in the flow direction for velocity and pressure drop as follows [41]:

$$u(x) = u(x+L) = u(x+2L) = \cdots \tag{9}$$

$$p(x) - p(x+L) = p(x+L) - p(x+2L) = \cdots . \tag{10}$$

Because the unit-cell is translationally periodic but not symmetric along the side walls, periodic boundary conditions are also applied to the lateral unit-cell boundaries. Using symmetric lateral boundary conditions was found to cause a non-physical temperature gradient perpendicular to the flow direction.

A uniform wall temperature, T_s, and no-slip condition are applied to the LFM solid-fluid interfaces. The analysis therefore assumes that the fins are perfectly conducting, and hence the Nusselt number obtained is dependent only on the flow geometry. This approach yields results that are independent of the ligament material thermal conductivity and is routinely employed for heat exchanger design. These results can then be more generally applied to any finite-conductivity surface by separately calculating an overall surface efficiency.

3.4. Surface efficiency correction

To account for the decreased effectiveness of the extended surface due to a temperature drop along the ligaments, we propose a simplified approach for calculating the overall surface efficiency for a tetrahedral LFM. The overall surface efficiency, η_o, is given by

$$\eta_o = 1 - \frac{A_f}{A_t}(1 - \eta_f), \tag{11}$$

where A_f is fin surface area and A_t is the total heat transfer area, including both the fin (ligament) and base surface areas. The analytical expressions for these two areas are given in Appendix A. The fin efficiency, η_f, is approximated by treating the ligament of the tetrahedral LFM as two fins, each half the ligament length

$$l_f = \frac{3}{2\sqrt{6}}H , \tag{12}$$

7

such that the fin tips can be assumed to be adiabatic based on symmetry. We then use the fin efficiency for a straight fin with constant cross-sectional area and an adiabatic tip, where the fin convection coefficient is calculated using Hilpert's correlation for a cylinder in cross flow [42]. The Hilpert equation uses the fin diameter, *i.e.,* the ligament diameter, d, as the characteristic length for the both the Nusselt and Reynolds numbers, and the superficial fluid velocity for determining the Reynolds number. The periodic unit-cell simulation results are corrected using this overall surface efficiency by multiplying the simulated Nusselt number by η_o. This simplified correction is demonstrated to provide reasonable agreement with a conjugate heat transfer simulation that includes conduction in the solid ligaments, as described in Appendix A.

3.5. Solution procedure and grid independence

The parameterized unit-cell geometries and meshes for this work are generated using the commercial software package CUBIT [43]. The cylindrical ligaments are first created to form the desired LFM structure, and these ligaments are subtracted from the cuboidal unit-cell to obtain the fluid domain. This fluid domain is then discretized into an initial mesh of approximately 750,000 tetrahedral elements that is biased to increase concentration of elements around the ligaments (Figure 2b). The mesh is imported into ANSYS Fluent [44] to solve the governing equations described in Section 3.2. Pressure-velocity coupling is accomplished via the SIMPLE algorithm [45] for solving the incompressible Navier-Stokes equations. Convergence is reached when the relative residuals drop below 10^{-5} for the continuity and momentum equations and 10^{-12} for the energy equation.

Grid independence is achieved through successive refinement of the mesh. The governing equations are solved on the initial mesh until the convergence criteria are met. The mesh is then locally refined based on the magnitude of velocity and temperature gradients. This solution refinement process is iterated upon until the fluid mass flow rate and average temperature change less than 1% between successive refinements. This typically required four refinements, with a maximum of six refinements for any given case; fully refined meshes typically contained 1.5 to 2.5 million elements, depending on the flow velocity. Figure 2c shows the fully refined mesh for a 95% porosity LFM at a prescribed pressure gradient of 40 Pa/m. Extensive refinement in regions downstream of the ligaments is visible in the final mesh with respect to the initial mesh shown in Figure 2b.

Each fully converged simulation provides the volume-averaged fluid temperature and mass flow rate through a LFM at a single porosity and pressure gradient. The flow rate is then used to calculate the friction factor and the Reynolds number for each case. The heat transfer coefficient is defined as

8

$$h = \frac{q''_{avg}}{T_s - T_{g,avg}} \quad ,$$ (13)

where $T_{g,avg}$ is the volume-averaged fluid temperature and q''_{avg} is the average heat flux over the entire solid–fluid interface area, as acquired from the simulation result. This convection coefficient is then used to calculate the Nusselt number.

4. Experimental approach

Experiments are performed to measure the hydraulic and thermal convection characteristics of lattice-frame materials to validate the modeling approach.

4.1. Samples

Two different tetrahedral LFM sample types are used to characterize the friction factor and Nusselt number. Samples for characterizing the friction factor are 3D printed (Stratasys, Eden 350V) using a low-conductivity acrylic-based photopolymer material (Fullcure 720) at four porosities of 75%, 85%, 90%, and 95%, as shown in Figure 3. These test samples are 11 mm × 147 mm × 127 mm in height, width, and length, respectively (1 unit-cell high, 12.6 unit-cells wide, and 9.5 unit-cells long). The printing resolution is ±26 μm, or ±2% of the smallest diameter ligament printed. For determining the Nusselt number, the sample is a 95% porosity 3D printed (ExOne, ±30 μm resolution) matrix of 420 stainless steel and bronze (Figure 3b). The thermal conductivity of the metal matrix is 22.6 W/(m K) [46]. The thermal test sample is slightly longer (134.7 mm; 10 unit-cells) and has 5 mm-thick top/bottoms walls for insertion of the thermocouples.

4.2. Experimental facility

The experimental facility (Figure 4) consists of four primary streamwise sections: an inlet contraction, a rectangular flow channel that holds the test sample, an outlet contraction, and an air suction system. Air is drawn from ambient conditions (21.5 °C, 101.3 kPa) through the inlet contraction (9:1) into the straight rectangular channel that houses the test sample. The 25-cm portion of the straight channel upstream of the test LFM sample is intended to ensure that well-conditioned laminar flow enters the sample. The outlet contraction interfaces the rectangular channel with the stainless steel piping of the air suction system. This downstream air system comprises a ring compressor (Fuji Electric, VFG504A-7W), a ball valve to control flow rate, and a volumetric flow meter (Omega, FMA1842A, 0 to 100 L/min range and ±1.13% full-scale range uncertainty). An absolute pressure transducer and thermocouple are used to obtain the air properties at the location of the flow meter in order to accurately determine the mass flow rate through the sample. Given the negligible uncertainty in the fluid properties and hydraulic

9

diameter, the Reynolds number uncertainty is calculated using the flow meter sensor uncertainty for each of the samples tested, as listed in Table 2.

The facility can be configured to perform either hydraulic or thermal experiments depending on the test sample that is installed in the rectangular flow channel. Figure 4 shows the experimental facility in both the hydraulic and thermal testing configurations. The rectangular flow channels for both configurations contain a section where the LFM sample is placed. A differential pressure transducer (Omega, PX655-0.1DI, 0 to 25 Pa; PX655-01DI, 0 to 250 Pa, both ± 0.31% full-scale range uncertainty) measures the pressure drop across the test sample using wall taps placed 25.4 mm upstream and downstream of the LFM sample. In the hydraulic testing flow channel (Figure 4c), a clamped acrylic top plate presses the LFM into contact with the bottom wall of the flow channel; to avoid any flow leakage, the interface between the top plate and channel wall is sealed with silicone RTV.

The rectangular flow channel for thermal experiments (Figure 4b) houses the LFM sample and heater assembly. Polyimide film heaters uniformly cover the top and bottom walls of the LFM sample. To ensure uniform heating, these heaters are attached with thermally conductive, double-sided tape (Thor Labs, TCDT2) to a 2 mm-thick copper plate heat spreader that is pressed against the LFM with a 2 mm-thick thermal interface pad (3M, Silicone Interface Pad 5591). An acrylic top plate compresses these layers to reduce the contact resistances.

The thermal testing configuration is instrumented with 32 T-type thermocouples. Rakes of four thermocouples each are placed across the upstream and downstream faces of the LFM sample to measure the inlet and outlet temperatures, respectively. These thermocouples are placed at four specifically chosen locations that represent four different geometric arrangements of ligaments so that the temperature measurements account for local variations in the temperature field in response to ligament arrangement (see insert in Figure 4a). Sheathed, ungrounded thermocouples are inserted to a depth of 25 mm from the side into the bottom wall of the LFM sample to measure the temperature at nine locations along the streamwise direction (see inset in Figure 4b); thermal paste is used to fill the clearance between the thermocouple probe and wall tap. Air-side temperatures in the LFM are measured at nine corresponding locations using thermocouples inserted vertically through the compression plate into the middle of the channel, equidistant from the top and bottom walls. Care is taken to ensure there is no contact between the thermocouple junctions and the ligaments. These air-side and wall thermocouples are placed at unit-cell length intervals of 13.5 mm along the streamwise direction, *i.e.*, each temperature measurement is taken at the same location with respect to the ligament arrangement. An array of six additional thermocouples is placed further downstream of the exit thermocouples to measure a thoroughly mixed outlet temperature. The ice-point referenced thermocouples are individually calibrated using a dry block

10

(Isotech Jupiter 650) and two factory-calibrated resistance temperature detectors (RTD, 60.1K), one each for the ice point and the dry block. Following calibration, the thermocouple temperature measurements have an absolute uncertainty of $\pm\, 0.3\,$°C.

4.3. Test Procedure

The hydraulic experiments are performed by recording the pressure drop across the LFM sample at known flow rates to determine friction factor as a function of Reynolds number. The flow rate is set manually by adjusting the ball valve; once the desired volumetric flow rate is obtained, the pressure drop across the sample is monitored until steady state operation is observed, and the pressure drop and flow rate are recorded (Agilent 34970A) at 1 Hz for 5 min. Pressure drop and volumetric flow rate data are averaged over this steady-state period at each flow rate and used to calculate the Reynolds number and friction factor, respectively. The uncertainty in the calculated friction factor is determined using the root sum of the squares method, accounting for both the sensor accuracy and the measurement precision (namely, the variance of measured temperatures and mass flow rate over the duration of the steady-state period).

The thermal experiments to determine Nusselt number as a function of Reynolds number are performed by recording the temperature difference between the gas stream and wall in the LFM sample at a known flow rate and heat flux. The flow rate is set manually by adjusting the ball valve, while the input power to the heaters is set by controlling the current through the heaters. Once the desired volumetric flow and heat input are set, the inlet, outlet, and streamwise temperatures are monitored for approximately two hours until steady state is observed, and then recorded at 1 Hz for an additional 30 min. Temperature measurements and volumetric flow rate data are averaged over the steady-state period. A second-order polynomial is fit to the time-averaged air temperatures versus streamwise position. The local heat flux is then calculated from the derivative of the least squares fit polynomial

$$q''(x) = \dot{m}c_p \frac{dT(x)}{dx} \ . \tag{14}$$

This accounts for non-uniform heat flux due to axial conduction through the walls of the LFM sample and heat-loss through the insulation. The local convection coefficient is then calculated as

$$h(x) = q''(x)\left(T_s(x) - T_g(x)\right), \tag{15}$$

where all quantities are functions of the axial position, x. This convection coefficient is then used to calculate the Nusselt number. The uncertainty in the convection coefficient is determined by the root sum of the squares method, again accounting for both the sensor accuracy and the measurement precision.

11

This uncertainty includes the uncertainty in the temperature gradient, dT/dx, determined from the 95% confidence interval of the least-squares fit polynomial coefficients.

5. Results

Unit-cell simulations were run for Reynolds numbers in the range $150 < Re < 1000$ at five distinct porosities: 75%, 85%, 90%, 95%, and 98%. The height of the tetrahedral structural unit was held constant at 11 mm for all simulations and experiments, and all other dimensions were calculated from this tetrahedron height (Table 3). The operating conditions for the experiments and simulations are summarized in Table 4. Hydraulic experiments using the polymer LFM samples were performed over the range of $200 < Re < 3500$, and are used to validate the friction factor calculated from the simulations as a function of Reynolds number. The experiments also reveal the Reynolds number at which the transition to turbulence occurs. The Nusselt number predictions were validated via thermal experiments using a single metal sample at $\varepsilon = 95\%$. The influence of porosity on the simulated Nusselt number and friction factor was assessed via several performance metrics.

5.1. Validation

A separate analysis was performed to evaluate whether the flow under the experimental conditions was hydraulically and thermally fully developed, so that the measured results may be compared to the unit-cell simulations. A conjugate heat transfer simulation of flow through the experimental test section, used to assess the entrance effects, is described in Appendix A. From these test-section simulation results we determine that the flow develops hydraulically within the first 20 mm of the experimental samples, *i.e.*, the flow is fully developed over 80% of the sample length. A direct comparison of the experimental pressure drop measurements with the unit-cell simulations is therefore reasonable, with an expectation that the measured pressure drop should be higher than that predicted by the fully-developed flow, unit-cell simulations. On the other hand, the test-section simulations indicate that the flow is still thermally developing, and an interpretation of the comparison of thermal measurements to the unit-cell simulations must take this into account.

5.1.1. Friction factor

Hydraulic experiments characterized the friction factor as a function of Reynolds number ($150 < Re < 3,500$) for all four test samples with porosities of 75%, 85%, 90%, and 95%, as shown in Figure 5. The friction factor initially decreases linearly with Reynolds number on a log-log scale up to $Re = 1,000$; this trend is characteristic of laminar flow. A transition to turbulence is indicated when the friction factor diverges from the trend in the laminar regime and begins to increase. This transition, where the friction factor reaches a local minimum, occurs at a consistent Reynolds number of approximately 1,000 for all porosities. As the Reynolds number increases beyond 1,000, the friction factor increases before again

12

decreasing. The unit-cell simulation results are plotted alongside the experimental data in Figure 5. Because the simulations were run with a laminar solver, no results are shown for Reynolds numbers greater than 1,000. The simulations and experiments show good agreement in the trends of friction factor versus Reynolds number within the laminar regime. As expected, the experimental data show a higher friction factor, especially at low Reynolds numbers where the entrance length will be longest.

5.1.2. Nusselt number

Thermal experiments were conducted for a single 95% porosity tetrahedral metal LFM sample. Figure 6 compares the measured local convection coefficient from experiments to the fully developed value from the unit-cell simulation. The convection coefficient from the unit cell simulations is corrected for the finite conductivity of the metal sample by multiplying the Nusselt number by the surface efficiency of the 22 W/(m K)-conductivity metal LFM sample as described in Section 3.4. The local heat transfer coefficient from a developing flow simulation of the full-length sample is also plotted for reference (see Appendix A). The experimentally measured convection coefficient decreases along the flow length, and begins to level out in the downstream end of the sample. This is consistent with the developing flow simulation which shows a decreasing trend throughout the sample length that appears to level-out near the end of the sample, ignoring the sharp drop in the last ~10 mm of the sample where the numerical boundary condition caused a sharp drop in the developing flow simulation. From both the experimental and simulated local convection coefficients, we conclude that the flow does not fully develop within the sample flow length, but it appears to converge to the fully developed value near the outlet of the sample. This is confirmed with a comparison to the fully developed flow solution predicted by the unit-cell simulation shown in Figure 6; the experimental convection coefficient is higher than the simulated value near the leading edge of the LFM sample, where entrance effects are most prominent, and converges toward the unit-cell simulation value near the downstream end of the sample, to within the experimental error. Following validation against the hydraulic and thermal experiments, all results presented henceforth are from the unit-cell simulations.

5.2. Performance metrics

The simulation results are analyzed using several surface goodness and performance metrics as a function of porosity. The values for these performance metrics are calculated from the unit-cell simulation results that assume perfectly conducting solid ligaments, and can be used to predict the performance of actual solid materials by accounting for a finite surface efficiency, as described in Section 3.3.

The friction factor and Nusselt number, plotted versus Reynolds number in Figure 7, are traditional performance metrics [40] that have been widely used in the literature to evaluate hydraulic and thermal

13

surface performance, respectively. The friction factor data are shown in Figure 7a, with the addition of the 98% porosity case with respect to Figure 5. As discussed previously in Section 5.1.1, the friction factor decreases with increasing fluid Reynolds number in a manner typical for laminar flow. The friction factor also decreases as the porosity decreases (*i.e.*, ligament diameter decreases) for the entire range of cases, as expected. The friction factor varies from $f = 4.0$ ($\varepsilon = 75\%$) to 1.8 ($\varepsilon = 98\%$) at the lowest Reynolds number, Re = 150, and from $f = 2.2$ ($\varepsilon = 75\%$) to 0.6 ($\varepsilon = 98\%$) at the highest Reynolds number, Re = 1000. This is an order of magnitude less than reported friction factors for metal foams of similar porosities (82% to 94%) [29]. The Nusselt number increases linearly with Reynolds number for all five porosities. The Nusselt number also monotonically increases as porosity decreases due to the increased surface area and flow mixing, indicative of improved heat transfer performance. Figure 8 shows contours of heat flux on the solid-fluid interfaces and velocity field vectors for several different porosities at a constant Reynolds number. The highest porosity case, 98%, shows a largely uniform velocity profile with minimal flow disturbances downstream of the ligaments, whereas the lowest porosity case, 75%, shows large disturbances with eddies forming downstream of the ligaments. The Nusselt number for the LFM cases, which ranges from 31 to 82 across all porosities and Reynolds numbers simulated, is similar to the performance reported for metal foams [29]. These results show that LFM structures can offer heat transfer performance that is comparable to metal foams, but at a significantly lower pressure drop. As an added benefit, LFM structures can bear ten times the load of metal foams at the same porosity [30].

Despite their wide use, these f–Re and Nu–Re curves vary greatly in magnitude and slope for different surface geometries, making comparison across different geometries difficult [48]. More importantly, compact heat exchanger surfaces must be optimized for pressure drop and heat transfer performance simultaneously. The ideal surface should yield both efficient heat transfer and low pumping power, and this must be accounted for in performance metrics for the design of multifunctional surfaces. This desire for optimized, multifunctional surfaces led to the development of other performance metrics, including the 'area goodness' [49], the 'volume goodness' [49, 50], and an 'efficiency index' [29].

The area goodness is defined as the Colburn j-factor factor divided by the friction factor, j / f. This area goodness is plotted as a function of Reynolds number in Figure 9a. At each porosity, j / f slightly decreases as a function of the Reynolds number. This functional dependence on Re is consistent with prior observations for complex flow geometries of non-constant cross section, in contrast with straight ducts for which j / f is constant [51]. The area goodness provides a measure of the frontal area required for a heat exchanger operating at a given design point (flow rate, pressure drop, and total surface area). This metric serves to minimize the flow area; the required frontal area of a heat exchanger is reduced for a higher j / f. However, the metric does not serve as an effective selection tool in most practical

14

applications where entire heat exchanger volume is also important. Without other such constraints, this performance metric drives the LFM structure toward an empty channel due to the low pressure drop (for an empty channel, $j / f = 0.35$) [51]. While this design would minimize the frontal area, the total heat exchanger volume would be much larger without any surface enhancements. Also, an empty channel cannot support structural loads. Thus, this design metric does not capture the inherent benefits of LFMs as a low-weight, multifunctional material.

The volume goodness is assessed by plotting the convection coefficient, h, against the friction power expended per unit of surface heat transfer area,

$$ E = \frac{1}{2} \frac{\mu^3}{\rho^2} \left(\frac{1}{2D_h} \right)^3 f \, \mathrm{Re}^3 . \tag{16} $$

Heat exchanger effectiveness is dependent on the number of transfer units for a fixed flow, which is proportional to hA_s if the thermal resistances of both sides of the heat exchanger are of the same order of magnitude. Thus, a higher h for a given E will yield a lower-volume heat exchanger, A_s [51]. An h–E plot is shown in Figure 9 for the simulated LFM structures, revealing a clear monotonic trend between porosity and h. The convection coefficient increases with decreasing porosity at any fixed E. Consequently, a larger ligament diameter will always yield a more desirable surface per this performance metric. However, this result does not consider applications in which weight is also of concern, where the design should be optimized for simultaneous reduction of both total heat exchanger volume and weight (in addition to maximizing heat transfer and minimizing pressure drop).

While the performance metrics above accounted for both pressure drop and thermal performance, a weighting based on the importance of these two interrelated effects must be chosen by the designer. A metric termed the efficiency index [29],

$$ \text{efficiency index} = \frac{\mathrm{Nu}}{f^{1/3}} , \tag{17} $$

was developed for comparing a wide range of extended surfaces from periodic cellular structures (*i.e.*, LFMs, louvered fins, and corrugated ducts) to stochastic metal foams and empty channels. The exponent of the friction factor is obtained from dimensional analysis such that pumping power and heat transferred are of equal magnitude across these differing geometries [29], though it does not consider the resulting heat exchanger size or weight. The predicted efficiency index for the tetrahedral LFM is plotted against Reynolds number in Figure 10. The efficiency index monotonically increases as the velocity increases for each porosity, and is a much stronger function of Reynolds number than of porosity. Throughout the laminar regime, there is no discernable difference between the intermediate three porosities (85%, 90%,

15

and 95%). At the low Reynolds numbers, the 75% porosity sample provides a modest improvement over all other porosities (~2 to 7% for Re < 600); as the Reynolds number increases, however, the 75% sample trends back toward the intermediate porosities. The highest porosity sample (98%) has a significantly lower efficiency index (*e.g.*, 11% at Re = 1000) compared to all other porosities. While the efficiency index weighs the interrelated effects on pressure drop and heat transfer, it does not predict an optimum porosity for this structure, but rather favors increasingly low porosities.

6. Conclusions

A unit-cell simulation approach was used to model the fully developed flow and heat transfer in tetrahedral LFM structures. This approach was validated by comparing to experimental measurements of the friction factor and Nusselt number for a subset of the cases; a simplified correction factor was used to account for the finite surface efficiency, which can be used to predict the thermal performance for materials of differing thermal conductivity based on the simulation data. The simulation test matrix results were used to compute several performance metrics of interest. These metrics were used to study the effect of porosity on performance, and the implications of each metric on the design of LFM heat exchangers discussed. The analysis illustrates the difficulty in arriving at any one universal performance metric for compact heat exchanger design. Simple performance metrics such as the friction factor or Nusselt number only consider hydraulic or thermal performance, respectively, and would drive the design toward unrealistic extremes. LFMs combine several benefits of high-porosity and surface area-to-volume ratio materials like metal foams, with much lower pressure drops and much higher structural integrity. To reflect the multifunctional design constraints of practical applications, we evaluate LFM performance using three metrics, namely, area goodness, volume goodness, and an efficiency index, that account for thermal and hydraulic performance simultaneously via different weighting of the thermal and hydraulic performance. This provides validated performance results spanning the laminar flow regime in tetrahedral LFMs that engineers can use to select an LFM heat exchange surface for improved performance under multifaceted design constraints.

16

Appendix A. Supplementary Data

Supplementary data associated with this article can be found in the online version.

References

1. S. Mahjoob, K. Vafai, A synthesis of fluid and thermal transport models for metal foam heat exchangers, *International Journal of Heat and Mass Transfer* **51** (15–16) (2008) 3701–3711.
2. P. Duplessis, A. Montillet, J. Comiti, J. Legrand, Pressure-drop prediction for flow-through high-porosity metallic foams, *Chemical Engineering Science* **49** (21) (1994) 3545–3553.
3. J.-F. Despois, A. Mortensen, Permeability of open-pore microcellular materials, *Acta Materialia* **53** (5) (2005) 1381–1388.
4. Y. Mahmoudi, M. Maerefat, Analytical investigation of heat transfer enhancement in a channel partially filled with a porous material under local thermal non-equilibrium condition, *International Journal of Thermal Sciences* **50** (12) (2011) 2386–2401.
5. Y. Su, J. H. Davidson, F. A. Kulacki, A geometry factor for natural convection in open cell metal foam, *International Journal of Heat and Mass Transfer* **62** (2013) 697–710.
6. M. Zafari, M. Panjepour, M. D. Emami, M. Meratian, Microtomography-based numerical simulation of fluid flow and heat transfer in open cell metal foams, *Applied Thermal Engineering* **80** (2015) 347–354.
7. V. V. Calmidi, R. L. Mahajan, Forced convection in high porosity metal foams, *Journal of Heat Transfer* **122** (3) (2000) 557–565.
8. K. Boomsma, D. Poulikakos, F. Zwick, Metal foams as compact high performance heat exchangers, *Mechanics of Materials* **35** (12) (2003) 1161–1176.
9. N. Dukhan, R. Picon-Feliciano, A. R. Alvarez-Hernandez, Air flow through compressed and uncompressed aluminum foam: Measurements and correlations, *Journal of Fluids Engineering* **128** (5) (2006) 1004–1012.
10. L. W. Jin, K. C. Leong, Pressure drop and friction factor of steady and oscillating flows in open-cell porous media, *Transport in Porous Media* **72** (1) (2008) 37–52
11. I. Kurtbas, N. Celik, Experimental investigation of forced and mixed convection heat transfer in a foam-filled horizontal rectangular channel, *International Journal of Heat and Mass Transfer* **52** (5–6) (2009) 1313–1325.
12. I. Kurtbas, N. Celik, I. Dincer, Exergy transfer in a porous rectangular channel, *Energy* **35** (1) (2010) 451–460.
13. A. A. Sertkaya, K. Altinisik, K. Dincer, Experimental investigation of thermal performance of aluminum finned heat exchangers and open-cell aluminum foam heat exchangers, *Experimental Thermal and Fluid Science* **36** (2012) 86–92.
14. A. Muley, C. Kiser, B. Sundén, R. K. Shah, Foam heat exchangers: a technology assessment, *Heat Transfer Engineering* **33** (1) (2012) 42–51.
15. S.-H. Park, T. H. Kim, J. H. Jeong, Experimental investigation of the convective heat transfer coefficient for open-cell porous metal fins at low Reynolds numbers, *International Journal of Heat and Mass Transfer* **100** (2016) 608–614.
16. G. B. Abadi, C. Moon, K. C. Kim, Experimental study on single-phase heat transfer and pressure drop of refrigerants in a plate heat exchanger with metal-foam-filled channels, *Applied Thermal Engineering* **102** (2016) 423–431.
17. C. Y. Zhao, Review on thermal transport in high porosity cellular metal foams with open cells, *International Journal of Heat and Mass Transfer* **55** (13–14) (2012) 3618–3632.
18. V. V. Calmidi, R. L. Mahajan, The effective thermal conductivity of high porosity fibrous metal foams, *Journal of Heat Transfer* **121** (2) (1999) 466–471.
19. J. W. Paek, B. H. Kang, S. Y. Kim, J. M. Hyun, Effective thermal conductivity and permeability of aluminum foam materials, *International Journal of Thermophysics* **21** (2) (2000) 453–464.

17

20. E. N. Schmierer, A. Razani, Self-consistent open-celled metal foam model for thermal applications, *Journal of Heat Transfer* **128** (11) (2006) 1194.
21. J. Kou, F. Wu, H. Lu, Y. Xu, F. Song, The effective thermal conductivity of porous media based on statistical self-similarity, *Physics Letters A* **374** (1) (2009) 62–65.
22. R. Dyga, S. Witczak, Investigation of effective thermal conductivity aluminum foams, *Procedia Engineering* **42** (2012) 1088–1099.
23. S. Y. Kim, J. W. Paek, B. H. Kang, Flow and heat transfer correlations for porous fin in a plate-fin heat exchanger, *Journal of Heat Transfer* **122** (3) (2000) 572–578.
24. A. Bhattacharya, R. L. Mahajan, Finned Metal Foam Heat Sinks for Electronics Cooling in Forced Convection, *Journal of Electronic Packaging* **124** (3) (2002) 155–163.
25. F. García-Moreno, Commercial applications of metal foams: their properties and production, *Materials* **9** (85) (2016).
26. B. Sundén and J. Fu, *Heat Transfer in Aerospace Applications*. London, UK: Academic Press, 2016.
27. L. Gao, S. Sun, Y. Zhao, Y. Sun, "Thermostructural multiobjective optimization of a composite sandwich panel with lattice truss cores," *Numerical Heat Transfer, Part B: Fundamentals* **70** (3) (2016) 233–250.
28. H. N. G. Wadley, Multifunctional periodic cellular metals, *Philosophical Transactions of the Royal Society of London A* **364** (1838) (2006) 31–68.
29. T. J. Lu, L. Valdevit, A. G. Evans, Active cooling by metallic sandwich structures with periodic cores, *Progress in Materials Science* **50** (7) (2005) 789–815.
30. J. Tian, T. Kim, T. J. Lu, H. P. Hodson, D. T. Queheillalt, D. J. Sypeck, H. N. G. Wadley, The effects of topology upon fluid-flow and heat-transfer within cellular copper structures, *International Journal of Heat and Mass Transfer* **47** (14–16) (2004) 3171–3186.
31. J. Xiong, R. Mines, R. Ghosh, A. Vaziri, L. Ma, A. Ohrndorf, H.-J. Christ, L. Wu, Advanced Micro-Lattice Materials, *Advanced Engineering Materials* **17** (9) (2015) 1253–1264.
32. J.-S. Liu, T. J. Lu, Multi-objective and multi-loading optimization of ultralightweight truss materials, *International Journal of Solids and Structures* **41** (3–4) (2004) 619–635.
33. S. Hyun, A. M. Karlsson, S. Torquato, A. G. Evans, Simulated properties of Kagomé and tetragonal truss core panels, *International Journal of Solids and Structures* **40** (25) (2003) 6989–6998.
34. J. Wang, A. G. Evans, K. Dharmasena, H. N. G. Wadley, On the performance of truss panels with Kagomé cores, *International Journal of Solids and Structures* **40** (25) (2003) 6981–6988.
35. G. W. Kooistra, V. S. Deshpande, H. N. G. Wadley, Compressive behavior of age hardenable tetrahedral lattice truss structures made from aluminium, *Acta Materialia* **52** (14) (2004) 4229–4237.
36. B.-K. Lee, K.-J. Kang, A parametric study on compressive characteristics of wire-woven bulk kagome truss cores, *Composite Structures* **92** (2) (2010) 445–453.
37. S. G. Krishnan, K. K. Bodla, J. A. Weibel, S. V. Garimella, Numerical investigation of fluid flow and heat transfer in periodic porous lattice-flame materials, *Proceedings of the fifteenth International Heat Transfer Conference,* Kyoto, Japan, 2014.
38. T. Kim, C. Y. Zhao, T. J. Lu, H. P. Hodson, Convective heat dissipation with lattice-frame materials, *Mechanics of Materials* **36** (8) (2004) 767–780.
39. T. Kim, H. P. Hodson, T. J. Lu, Fluid-flow and endwall heat-transfer characteristics of an ultralight lattice-frame material, *International Journal of Heat and Mass Transfer* **47** (6–7) (2004) 1129–1140.
40. T. Kim, H. P. Hodson, T. J. Lu, Pressure loss and heat transfer mechanisms in a lattice-frame structured heat exchanger, *Proceedings of the Institution of Mechanical Engineers* **218** (11) (2004) 1321–1336.
41. W. M. Kays, A. L. London, *Compact Heat Exchangers*, 3 edition. Malabar, Fla: Krieger Pub Co, 1998.
42. S. Krishnan, S. V. Garimella, J. Y. Murthy, Simulation of thermal transport in open-cell metal foams: effect of periodic unit-cell structure, *Journal of Heat Transfer* **130** (2) (2008) 024503–024503.
43. F. P. Incropera, D. P. DeWitt, *Fundamentals of Heat and Mass Transfer*, sixth ed., Wiley, Hoboken, NJ, 2006.

18

44. CUBIT, version 13.0 [computer software]. Sandia National Laboratory, Albuquerque, NM, 2011.
45. Fluent, version 15.1 [computer software]. ANSYS-Fluent Inc., Cannonsburg, PA, 2013.
46. S. Patankar, *Numerical Heat Transfer and Fluid Flow*, first ed. CRC Press, New York, 1980.
47. Material Data Sheet: 420 Stainless Steel Infiltrated with Bronze. ExOne, North Huntingdon, PA, 2014, pp. 2.
48. H. N. G. Wadley, N. A. Fleck, A. G. Evans, *Fabrication and structural performance of periodic cellular metal sandwich structures* **63** (2003) 2331-2343.
49. P. G. LaHaye, F. J. Neugebauer, R. K. Sakhuja, A generalized prediction of heat transfer surfaces, *Journal of Heat Transfer* 96 (4) (1974) 511–517.
50. A. L. London, Compact heat exchangers, Part 2 - surface geometry, *Mechanical Engineering* 86 (6) (1964) 31–34.
51. A. L. London, Ferguson, C. K., Test results of high-performance heat exchanger surfaces used in aircraft intercoolers and their significance for gas-turbine regenerator design, *Transactions of ASME* 71 (1949) 17–26.
52. R. K. Shah, A. L. London, *Laminar Flow Forced Convection in Ducts: A Source Book for Compact Heat Exchanger Analytical Data*. Academic Press, 1978.

19

List of tables

List of figures

Table 1. Geometric definitions of tetrahedral lattice-frame material structural units and periodic unit cells.

parameter	symbol	geometric definition
ligament length	l	$\dfrac{\sqrt{6}}{2}H$
angle between ligament and base	ϕ	$\sin^{-1}\dfrac{H}{l}$
longitudinal pitch	S_x	$\dfrac{\sqrt{6}}{2}H$
transverse pitch	S_y	$\dfrac{3\sqrt{2}}{4}H$

Table 2. Ligament diameter and hydraulic diameter for the simulated LFM geometries; for the porosities that were experimentally characterized, the uncertainty in Reynolds number is also provided.

porosity, ε	ligament diameter, d / [mm]	hydraulic diameter, D_h / [mm]	Reynolds number uncertainty
75%	4.18	8.19	9.4
85%	3.13	9.19	11.5
90%	2.50	11.2	12.8
95%	1.73	13.2	15.1
98%	1.07	15.5	N/A

Table 3. Dimensions of tetrahedral lattice-frame material structural units and simulation domain of the periodic unit cell.

tetrahedral structural unit	
longitudinal pitch (S_x)	13.5 mm
transverse pitch (S_y)	11.7 mm
height (*H*)	11 mm
periodic unit cell	
Length (*L*)	26.9 mm
Width (*W*)	23.3 mm
Height (*H*)	11 mm

Table 4. Experimental and simulated operating conditions.

parameter	experiment	simulation
inlet temperature, K	294.7	300
inlet pressure, kPa	101.3	101.3
superficial velocities, m/s	0.05 – 1.00	0.05 – 0.80
porosity range	75% - 95%	75% - 98%
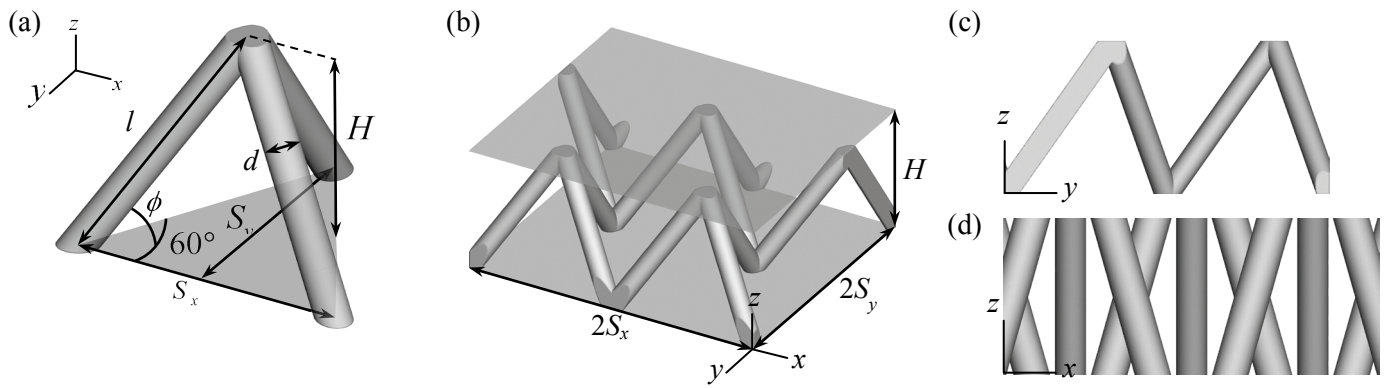
Figure 1. (a) Basic structural unit of a tetrahedral lattice-frame material and (b) a periodic unit-cell containing four basic structural units with important dimensions overlaid. Frontal views of periodic unit-cell are shown as viewed from the (c) low-blockage and (d) high-blockage orthogonal orientations.
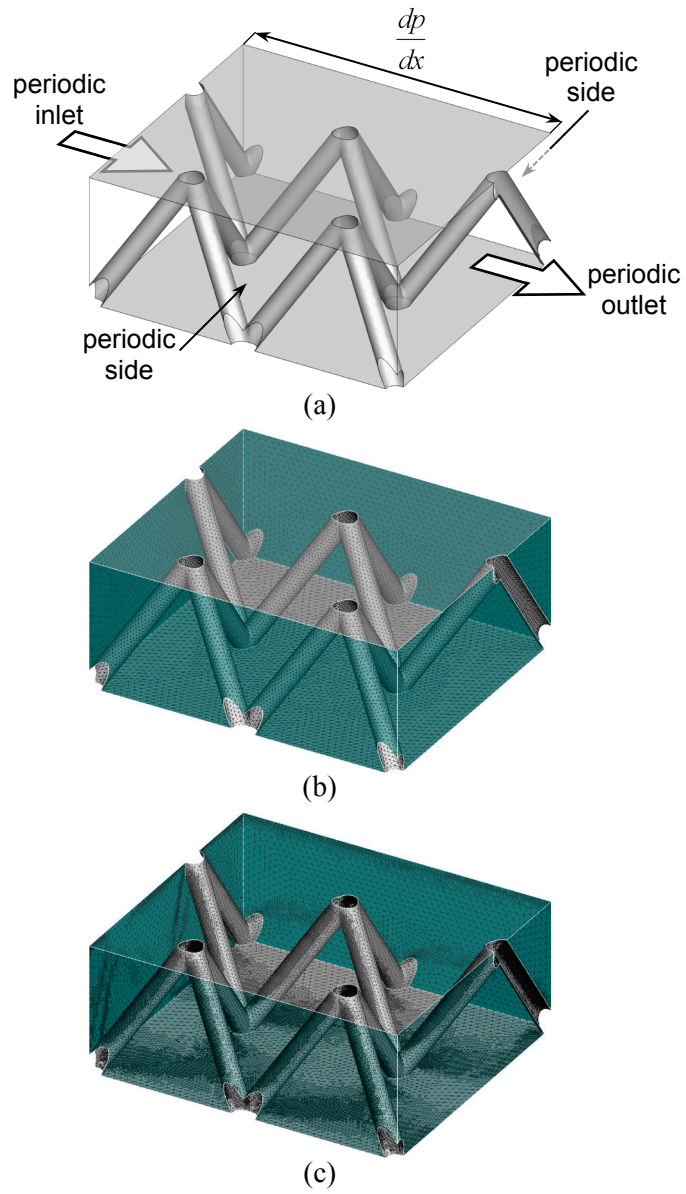
Figure 2. Computational domain for 95% porosity tetrahedral lattice-frame material showing (a) the flow domain boundary conditions employed, (b) the initial mesh before any refinements, and (c) the fully refined mesh for a converged solution at $dp/dx = 40$ Pa/m (Re = 978).
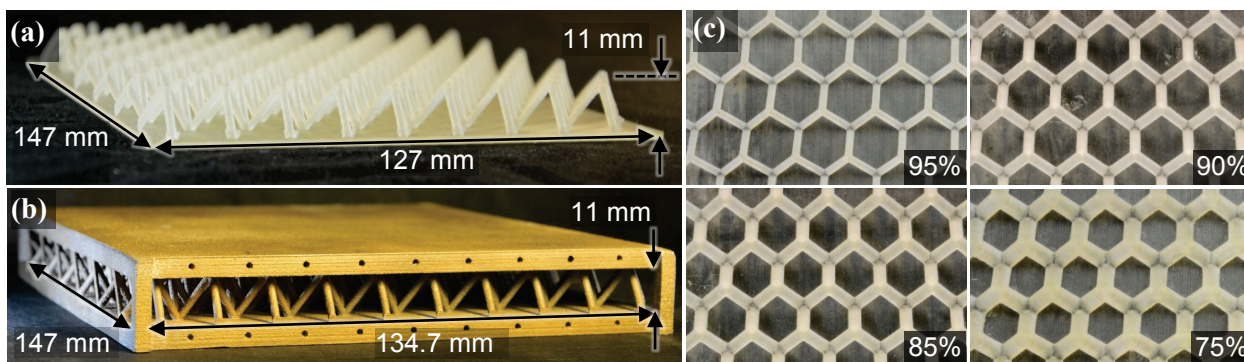
Figure 3. Photographs of 95% porosity tetrahedral (a) polymer and (b) metal LFM samples used for hydraulic experiments and thermal experiments, respectively; (c) a top-down view of the LFM structure is shown for the samples of differing porosity used for hydraulic testing.
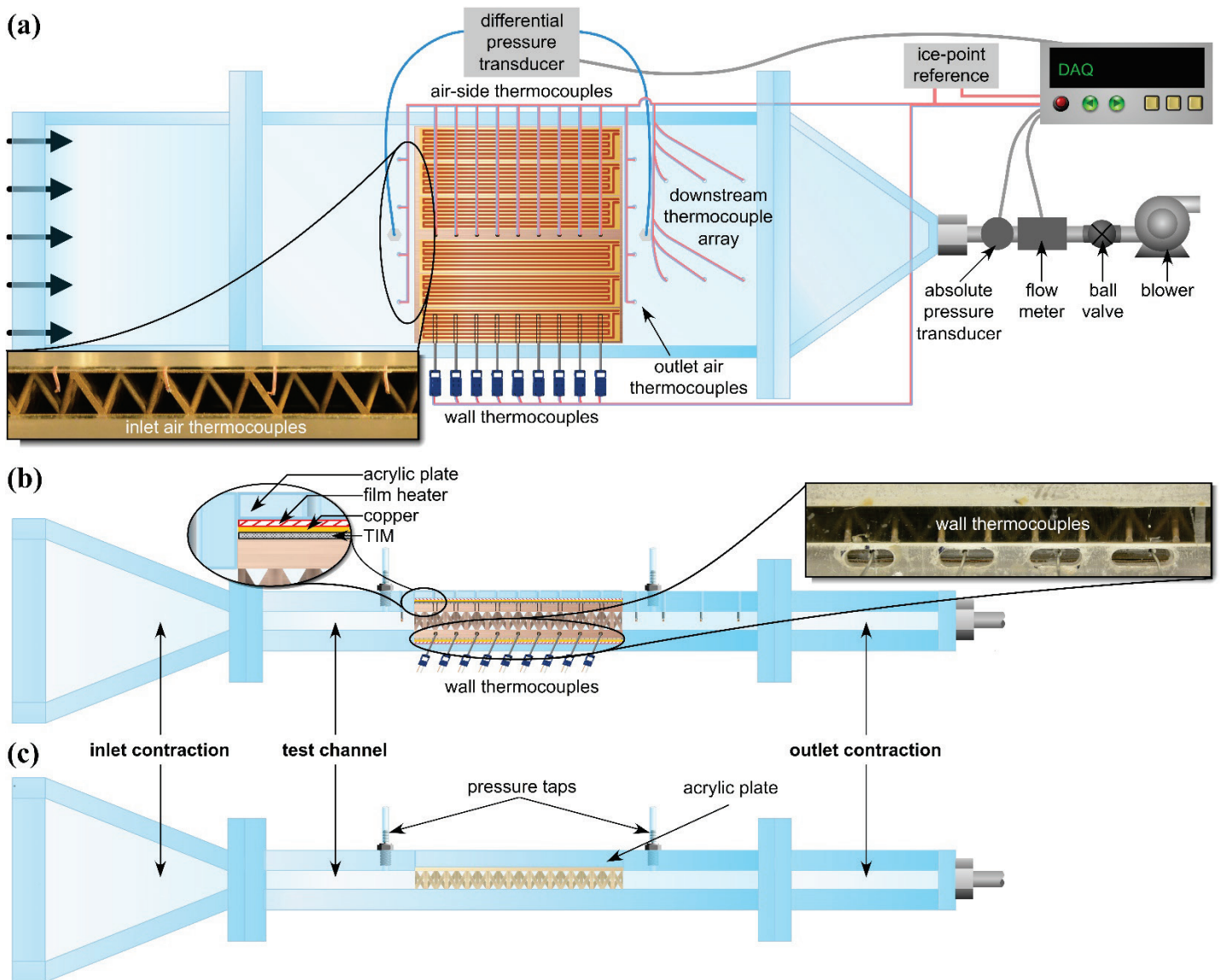
Figure 4. (a) Schematic diagram of experimental facility showing flow path (left to right) and instrumentation. Two different configurations of the test channels are shown for (b) thermal and (c) hydraulic experiments. All thermocouple wiring is shown as blue–red lines, with inset photographs showing the placement of the inlet air thermocouples and wall thermocouples inserted into the base of the LFM sample.

29
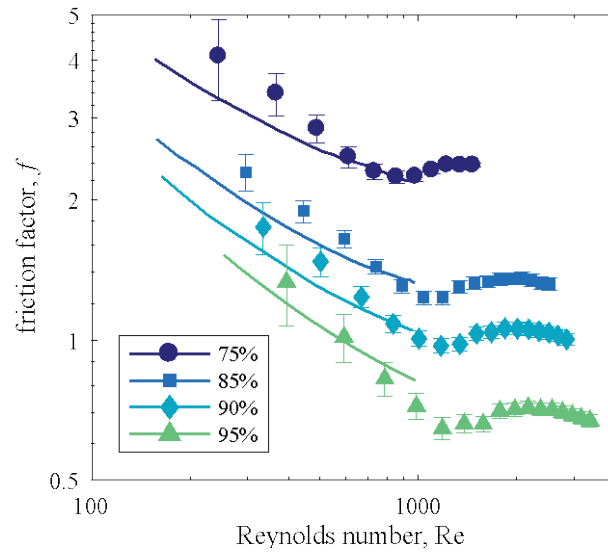
Figure 5. Friction factor plotted as a function of Reynolds number from experimental measurements (symbols with error bars) and unit-cell simulation results (solid lines) for tetrahedral LFM at four porosities.
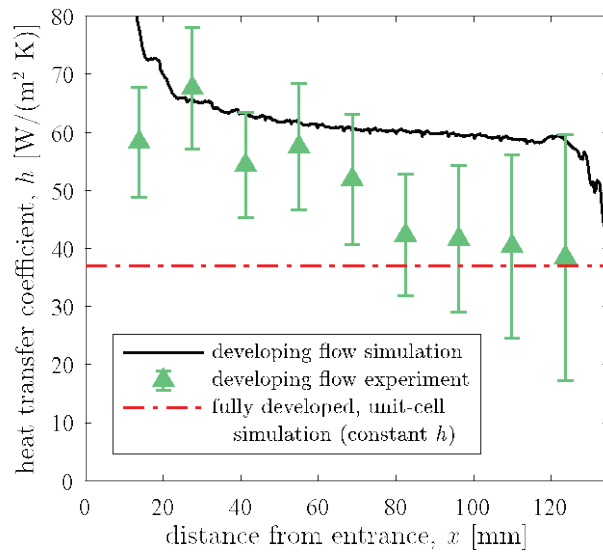
Figure 6. Heat transfer coefficient plotted as a function axial position from the experiments (green triangles) and developing-flow simulation (solid black line). Predicted convection coefficient for fully developed flow, from the unit-cell simulation, is shown comparison (red dashed line).
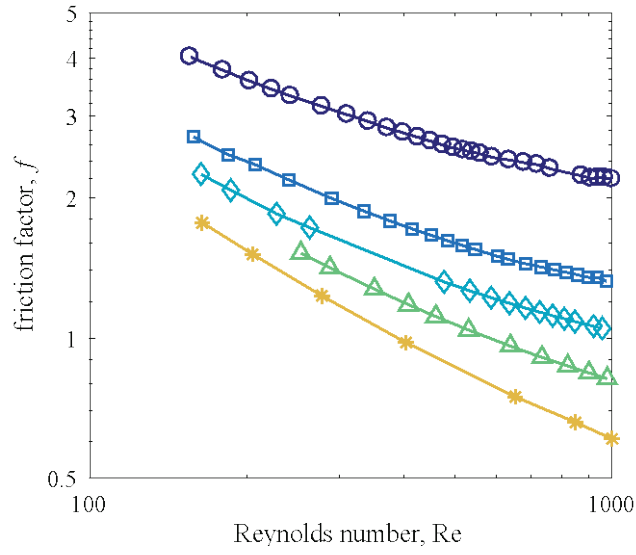
(a)
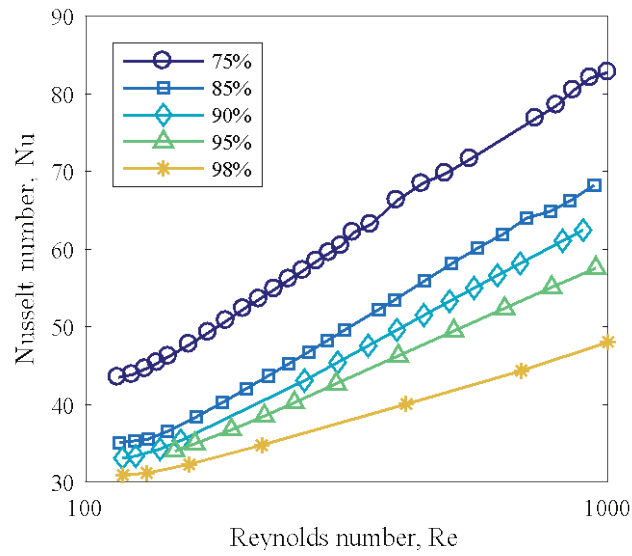
(b)

Figure 7. (a) Friction factor and (b) Nusselt number versus Reynolds number calculated from unit-cell simulations of a tetrahedral LFM at five porosities.
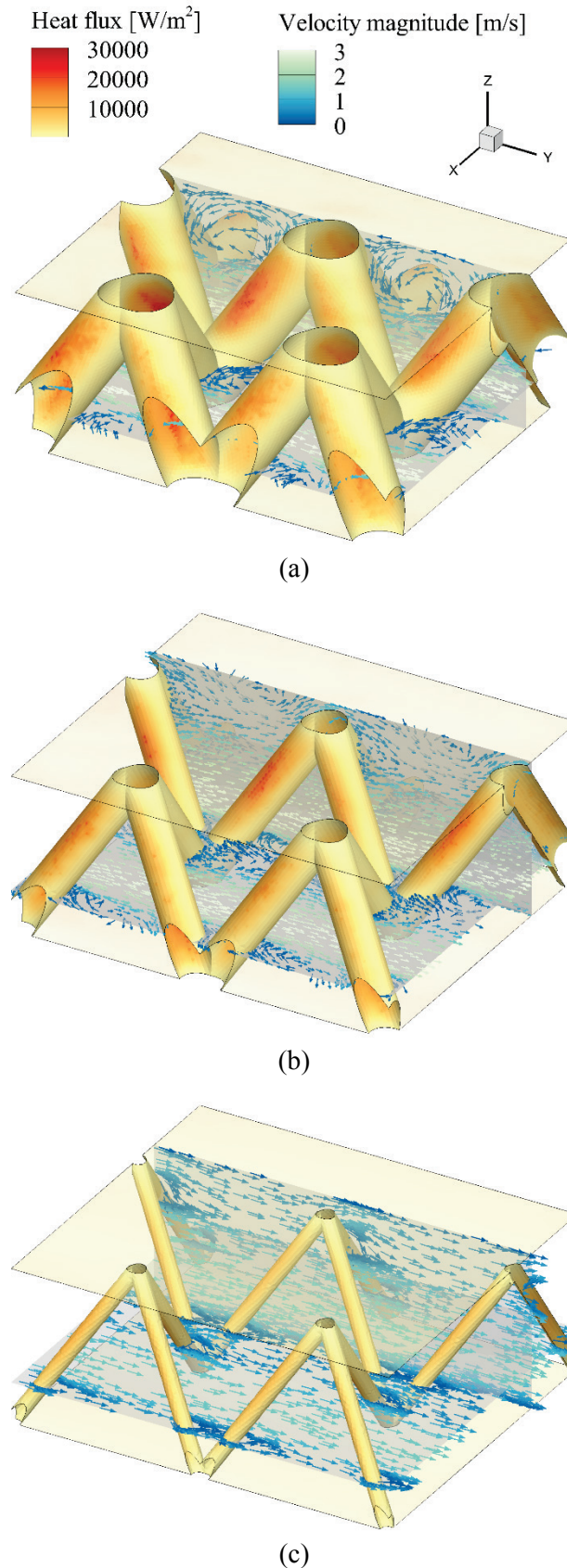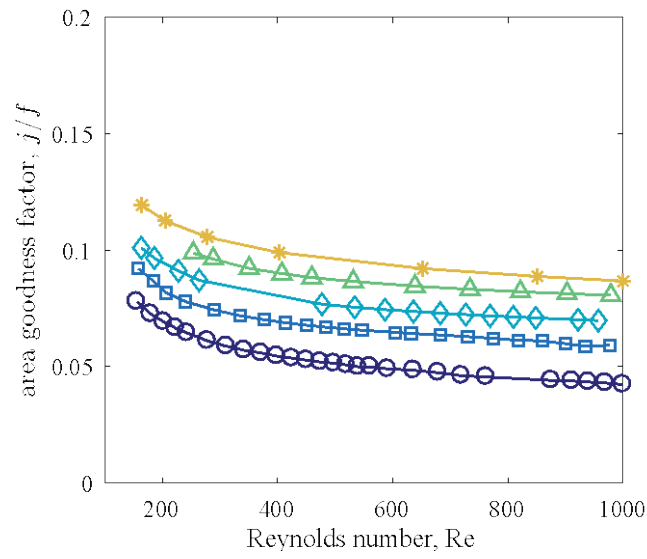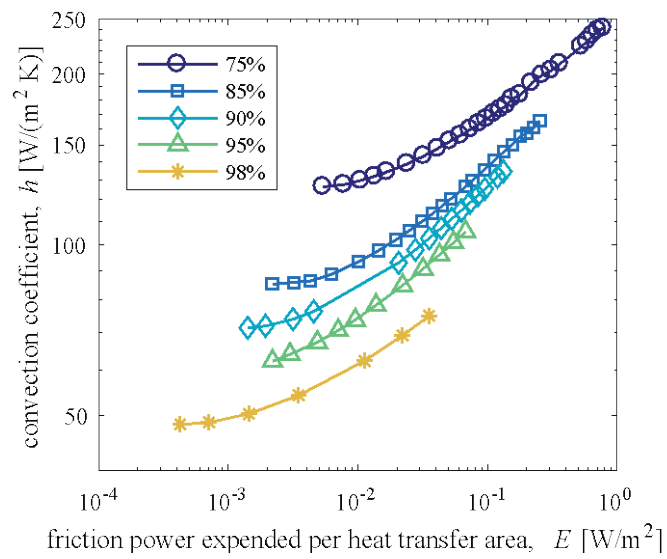
Figure 8. Contours of the heat flux on solid-fluid interfaces with velocity vectors shown on *x*-plane and *z*-plane slices at Re ≈ 620 for ε = (a) 75%, (b) 90%, and (c) 98%.

(a)

(b)

Figure 9. (a) Area goodness and (b) volume goodness factors calculated from unit-cell simulations of a tetrahedral LFM at five porosities.
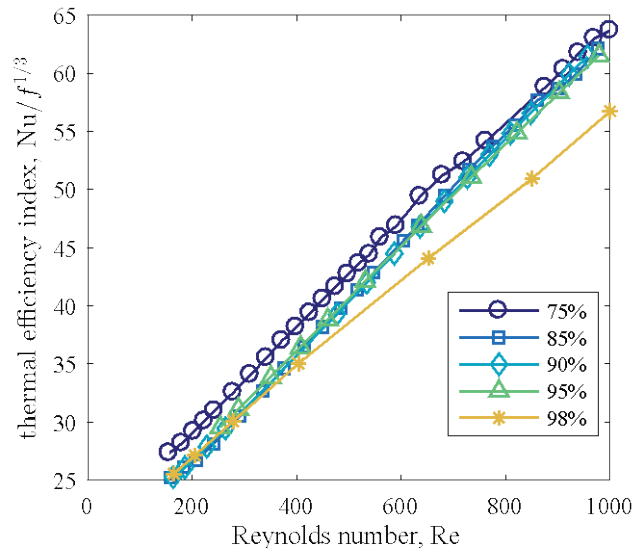
Figure 10. Efficiency index calculated from unit-cell simulations of a tetrahedral LFM at five porosities.